NANO LETTERS

pubs.acs.org/NanoLett
Letter

Controlling Plasmonic Catalysis via Strong Coupling with Electromagnetic Resonators

Jakub Fojt, Paul Erhart, and Christian Schäfer*

Cite This: *Nano Lett.* 2024, 24, 11913−11920
Read Online

ABSTRACT: Plasmonic excitations decay within femtoseconds, leaving nonthermal (often referred to as "hot") charge carriers behind that can be injected into molecular structures to trigger chemical reactions that are otherwise out of reach—a process known as plasmonic catalysis. In this Letter, we demonstrate that strong coupling between resonator structures and plasmonic nanoparticles can be used to control the spectral overlap between the plasmonic excitation energy and the charge injection energy into nearby molecules. Our atomistic description couples real-time density-functional theory self-consistently to an electromagnetic resonator structure via the radiation-reaction potential. Control over the resonator provides then an additional knob for nonintrusively enhancing plasmonic catalysis, here more than 6-fold, and dynamically reacting to deterioration of the catalyst—a new facet of modern catalysis.

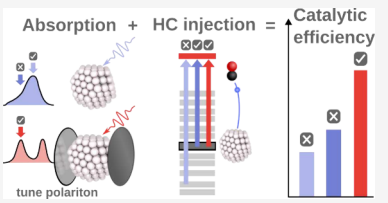

KEYWORDS: *Plasmonic Catalysis, Strong Light−Matter Coupling, Hot Carriers, Polaritonic Chemistry, Localized Surface Plasmon, Density-Functional Theory*

Hot carrier (HC) technology, i.e., injecting HCs (nonthermal carriers) into a molecule[1] or semiconductor,[2] promises considerable improvements in light-harvesting,[2] solar-to-chemical energy conversion,[3−5] and catalysis.[6−11] Commonly, HCs are generated in plasmonic nanoparticles (NPs) through the nonradiative decay of the localized surface plasmon (LSP), a mode of collective electronic motion that is excited by light. This process is highly efficient due to the large absorption cross section of plasmonic NPs at visible-near UV frequencies.[12−14] One possible process of injecting those generated HCs into a molecule follows a *direct* HC transfer[15] where charge-transfer excitations form with one carrier in the NP and the other in the orbital of a molecule. This "direct transfer/injection" is thus *not* sequential but directly creates HC in the molecule. We will use "HC injection" synonymously with this direct injection process in the following to stay consistent with the available literature. Such a direct process is more useful in terms of selectivity,[16] has been experimentally observed[17−19] and is at least as likely[15,19] as the process of transferring HCs that are formed in the NP across the interface.[6] The direct HC transfer process sensitively depends on the alignment of energetic levels comprising charge transfer and LSP excitations.[20] Improving HC generation and injection are therefore critical to explore the full potential of plasmonic catalysis.

One possible angle to improve plasmonic catalysis is to control the interplay between plasmonic particles and an optical field. Confining optical modes, may it be via structured meta-surfaces or Fabry-Pérot cavities, results in an increase in interaction to a material with spectral overlap. From an increase in mode density follows, according to Fermi's golden rule, an increase in photoabsorption cross section, which has been successfully employed to deposit more energy in plasmonic NPs, create more HCs, and thus further increase catalytic efficiency.[9,11,21−24] At sufficiently strong interaction, light and matter hybridize into polaritonic quasi-particles that can enhance exciton[25−29] or charge[30−33] conductance and even control chemical reactivity.[34−41] Plasmonic nanoparticle crystals[42,43] can reach extreme light-matter coupling strength, entering the deep strong coupling domain, that even exceeds the excitation energy of the LSP of the NPs comprising the crystal.

In this Letter, we explore to which extent strong coupling between an optical resonator and a plasmonic Ag NP can be leveraged to control the catalytic effect on a nearby CO molecule. Our approach is based on energetic restructuring, i.e., each step in the catalytic process is associated with a set of energies and the efficiency of the full process is optimized by aligning those energies. In contrast to strongly coupling the molecule to the NP, which is suggested to lead to minor changes in HC transfer,[44] our systems features strong coupling between the NP and the external resonator. Using an atomistic description of the NP-molecule system, we show that the microscopic mechanism of charge injection to the molecules is a dephasing of the LSP to charge-transfer excitations.[20,45,46] We then couple the system to an optical cavity,[47] giving rise to

Received: July 4, 2024
Revised: September 10, 2024
Accepted: September 10, 2024
Published: September 12, 2024

https://doi.org/10.1021/acs.nanolett.4c03153
Nano Lett. 2024, 24, 11913−11920

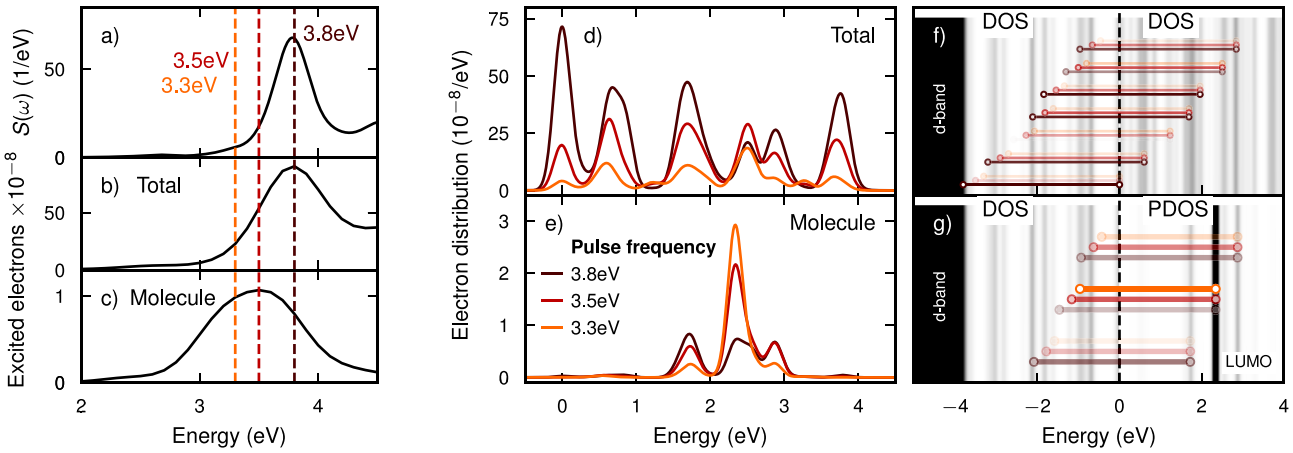

Figure 1. (a) Absorption spectrum of the NP-CO coupled system. The colors of the vertical dashed lines correspond to 3 exemplary excitation energies. (b) Number of excited electrons in the total system and (c) in the molecule. (d) Electron distribution in the total system and (e) projected on the molecule. (f) Schematic illustration of the energy-conserving excitations that contribute to excited electrons in total, overlaid on the total density of states (DOS). As there are many available states, there are many possibilities to satisfy the energy conservation condition (see text). (g) Schematic illustration of the energy-conserving excitations that contribute to excited electrons in the molecule, overlaid on the total DOS of unoccupied states and projected density of states (PDOS) of the molecule of unoccupied states. The sparse PDOS defines much stricter resonance conditions such that energetic matching becomes an essential component of catalytic efficiency. The opacity of the transitions in (f, g) is proportional to the relative probability of each particular excitation.

polaritonic states that emerge from hybridization of light and matter. The polaritonic states allow tuning of previously mismatched energies, providing nonintrusive control that increases the efficacy of HC injection into the molecule more than 6-fold. We conclude with a comprehensive discussion of potential applicability and limitations, including a comparative study for engineering the shape of the NP.

SYSTEM

Our exemplary model system comprises a CO molecule near a 201-atom Ag NP (effectively 1.5 nm in diameter; Figure S1a). The LSP of the NP (resonance at 3.8 eV; see Figure 1a) and molecular excitations have no spectral overlap. Carriers that form on the molecule are then only due to a photocatalytic effect of the excited LSP dephasing into charge-transfer excitations—providing unambiguous insight into the HC injection. We place the molecule 3 Å from the (111) face of the NP, as the alignment is most clearly illustrated here, but discuss other distances in the SI. We excite the system with light polarized along the bond axis of the molecule. A detailed description of methodology and dephasing process can be found in the SI and refs 20 and 46.

HOT-CARRIER TRANSFER

A prerequisite for the generation of HCs is the absorption of energy. It is therefore not surprising that when varying the frequency of the driving pulse, the number of excited electrons in the system (i.e., NP and molecule) roughly follows the shape of the absorption spectrum (Figure 1a, b), as the amount of energy absorbed dictates how many carriers are excited. However, the number of hot electrons (HEs) injected to the molecule clearly deviates from this shape (Figure 1c) as HC transfer depends on generation and *injection* efficiency. The maximum injection is obtained at 3.5 eV, which is off-resonant to the LSP, and the number of injected HCs is roughly constant in a range of pulse frequencies between 3.3 and 3.6 eV. Thus, factoring out the efficiency of absorption (77% less energy is absorbed using, e.g., the 3.3 eV pulse compared to 3.8 eV; see Figure S2) the injection of HEs must be much more efficient using a pulse of 3.3 eV.[20] In fact, by normalizing the number of injected carriers by the amount of energy absorbed at each pulse frequency (Figure 3; solid line), we construct a hypothetical injection efficiency that peaks at 3 eV. We return to discuss this later in the text. It should be pointed out that hot holes are also injected into the molecule, albeit to a much smaller extent (Figure S3), as the highest occupied molecular orbital (HOMO) is too far below the Fermi level given the pulse frequencies considered (Figure S4).

LEVEL ALIGNMENT

To understand why electron injection is more efficient off-resonance, let us give a perturbative perspective on HC generation. Driving the system with an external potential V_{ext} we perturb the density $\delta\rho$ and induce a potential δV. This is primarily the Coulomb potential of the LSP. HCs form as the LSP starts to decay,[46] as their coupling to V_{ext} is much weaker than to δV. From Fermi's golden rule we should expect a continuous drive of frequency ω to result in a rate of HE formation in state a to be $1/\tau/\hbar^2\sum_i(2-f_a)f_i|M_{ia}|^2 \cdot (1/[(\omega-\omega_{ia})^2+\tau^{-2}] + 1/[(\omega+\omega_{ia})^2+\tau^{-2}])$ where $\hbar\omega_{ia}$ is the energy of excitation $i \rightarrow a$, f_i and f_a occupation numbers (including spin degeneracy of 2) and τ a characteristic lifetime of carriers.[48] The denominator represents the requirement for energy-conservation during the excitation event, i.e., the longer the lifetime, the sharper the resonant condition.[a] The transition matrix element $M_{ia} = \int d\mathbf{r}(V_{ext} + \delta V[\delta\rho])(f_i - f_a)\psi_i^*(\mathbf{r})\psi_a(\mathbf{r})$ includes excitations driven directly by the external field and excitations driven by the induced density. The latter is the only non-negligble term of M_{ia}, and effectively represents the coupling strength of the LSP to each excitation times the coupling strength of the LSP to the driving field, through the dependence on $\delta\rho$.

Mapping out all excitations in the system (Figure S5) we see a competition between two effects dictating the probability for an excitation to occur. The pulse should be aligned to (i) the excitation energy ω_{ia} in order to satisfy the resonance

https://doi.org/10.1021/acs.nanolett.4c03153
Nano Lett. 2024, 24, 11913−11920

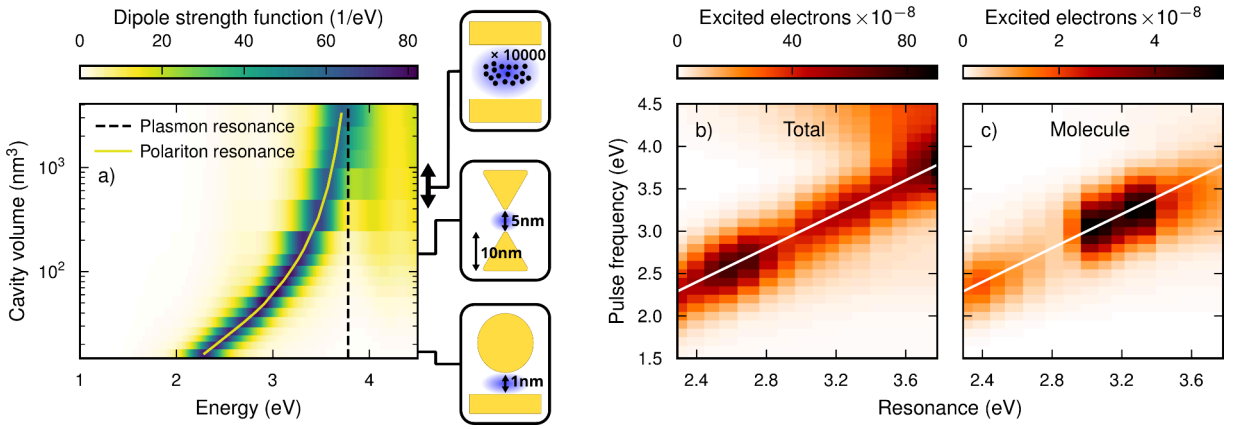

Figure 2. (a) Absorption spectrum of the NP-CO coupled system for different coupling strengths of the cavity. The spectral positions of the plasmon and the LP resonance are indicated by dashed and solid lines, respectively. The energetic position of the lower polariton (LP) resonance very closely follows the curve (3.805 eV − 6.2425 eVnm$^{3/2}$/$\sqrt{V}$), where V is the cavity volume. The sketches mark effective cavity volumes that are possible to realize using (from the top) optical/meta-surface cavities and collective strong coupling (example assuming $N = 10^4$, can be tuned by changing the density of emitters, further details in text), bow-tie antennas,[49] and nanocavities.[50] (b) Number of electrons excited in the system as a whole, (c) as well as in the molecule. The latter are plotted as a function of the spectral position of the resonance, which can be related to the cavity volume according to (a).

condition ($\sim 1/(\omega - \omega_{ia})^2$) and (ii) the LSP resonance, as $|M_{ia}(\omega)|^2$ scales with the amount of energy absorbed.

The total NP+molecule system involves many energy-conserving excitations due to the dense DOS of the NP (illustrated by the accordingly colored lines in Figure 1f), such that (i) plays a minor role and (ii) causes the HE distribution to rather uniformly decrease in amplitude when the pulse is detuned from the LSP (Figure 1d+b). However, only few energy-conserving *charge-transfer* excitations, i.e., from NP *to* molecule, exist (Figure 1g) due to the more discrete molecular level-structure. For our particular NP-molecule geometry, the lowest unoccupied molecular orbital (LUMO) is hybridized with the metal, forming three distinct states at 1.73, 2.33, and 2.87 eV above the Fermi level (Figure S4; note that there is also a less pronounced state at 2.53 eV). Across all pulse frequencies, an excitation from NP states at −0.93 eV to the middle orbital at 2.33 eV ($\hbar\omega_{ia}$ = 3.26 eV) contributes the most to electron transfer (Figure S5). The intensity of this excitation increases as the pulse frequency is tuned closer to 3.26 eV, thanks to the resonance condition, despite the absorption decreasing as the pulse is detuned from the LSP (3.8 eV). For a pulse frequency of 3.2 eV, this excitation makes up almost 40% of the electron transfer (almost 80% made up by just 10 excitations). In practice, computing a meaningful matrix element M_{ia} for this excitation is a nontrivial task, as HCs are formed continuously due to the time-dependent density due to the LSP. However, our current interpretation is that this excitation, and a few others, have particularly large matrix elements due to the overlap of the acceptor and donor wave functions with the potential from the LSP. An improved alignment to a few excitation energies (3.02, 3.26, and 3.54 eV among others; see Figure S5) as the pulse is red-detuned causes more HEs to be injected into the middle orbital 1.98 eV (Figure 1g). Competition with the alignment to the LSP (3.8 eV) as well as the presence of other charge-transfer excitations with different ω_{ia} ultimately causes the plateau in HE injection between 3.3 and 3.6 eV. Having control over the alignment criteria (i) and (ii) presents a clear way forward to optimize HC injection. We begin by exploring to which extent strong coupling to electromagnetic resonator structures can be used to tune polaritonic excitations and ultimately increase injection efficiency.

MODIFYING THE RESONANCE WITH STRONG COUPLING

We introduce a simplified representation of a lossy cavity mode[b] to our NP-molecule system via the radiation-reaction potential,[47] as demonstrated in ref 51. The frequency of the cavity mode is tuned to the LSP resonance of 3.8 eV and the mode features a lifetime of τ = 17.32 fs, which is longer but still comparable to the lifetime of the LSP. Energy is absorbed from the pulse only via the matter system to ensure comparable results for all following investigations, i.e., increasing absorption efficiency is a secondary effect of resonator structures that we do not discuss in this manuscript but that has been explored in previous experiments. Here, we use an unspecified cavity structure to explore our hypothesis but illustrate possible realizations with typical effective cavity volumes in the insets of Figure 2a. In addition to a realization where a single NP-molecule system is strongly coupled to a small resonator, our discussion can be transferred to the collective coupling regime in which an ensemble of N NP-molecule subsystems couples collectively to e.g. an optical Fabry-Pérot cavity. In the collective limit, the HC injection efficiency of each NP-molecule subsystem will be smaller by a factor $1/N$, but since an optical excitation is shared among N subsystems the total increase in catalytic efficiency of the entire system is identical to the simulations demonstrated in the following per absorbed photon ($N \times 1/N$, linear response theory).[c] The optical field follows Maxwell's equations which leaves the electronic Kohn−Sham orbitals, and therefore condition (i), unaffected. Strong interaction between cavity and LSP causes the LSP to split in lower polariton (LP) and upper polariton (UP) (Figure 2a; the latter, however, is quenched at large coupling strengths due to overlapping with interband transitions). The clue is now that the LP can be monotonically red-shifted by reducing the effective mode volume of the resonator structure or increasing the density of optical emitters inside a given volume—we control condition (ii) by controlling the cavity.

https://doi.org/10.1021/acs.nanolett.4c03153
Nano Lett. 2024, 24, 11913−11920

Unsurprisingly, the total number of excited electrons in the system peaks when the system is driven in resonance with the LP (Figure 2b). Slightly shifting the LP approximately halves the number of electrons in the total system as the LSP is split into two polaritonic states that carry each half of the oscillator strength. Further increasing the cavity strength, the number of excited electrons stays roughly constant, with a notable exception between 2.5 and 2.8 eV. We attribute the increase in this region to a spectral overlap of the LP with a feature in the spectrum at 2.6 eV (Figure 1a; compare spectra of larger NPs in ref 46.).

The number of electrons *injected* into the molecule does not necessarily peak at resonance, which we knew already from the no-cavity case. As illustrated in Figure 2, tuning the LP into the energetic domain of optimal injection efficiency at 3 eV results in a considerable increase of HEs injection. We increase the electron injection by a factor of 6.8 (the configurations with LP energy/pulse frequency of 3.02/3.0 eV, $V = 63.2$ nm^3, and LP energy/pulse frequency of 3.26/3.2 eV, $V = 131.2$ nm^3, tie for this record), compared to the cavity-free system excited at resonance (Figure 3; golden markers). Repeating this study for

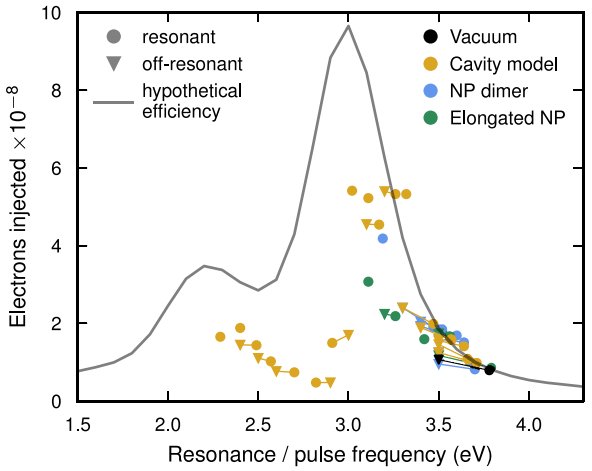

Figure 3. Number of electrons injected into the molecule for different setups. Because the principal charge-transfer excitation is red-detuned relative to the LSP resonance, transferring the most charge requires a trade-off between being tuned to the resonance (circles) and being tuned to the charge-transfer excitation. Imagining that we could "artificially" shift the resonance yields the solid gray line. The slight blue-shift of the in-cavity envelope and the artificially shifted resonance can be attributed to self-polarization effects.[47,52] The data is normalized to correspond to the same absorption as the 201-atom vacuum system. In particular, the values for the NP dimer have been halved, and the values for the elongated NPs have been multiplied by 201 and divided by the number of atoms in each structure.

other distances between the NP and molecule results in similar, although weaker, behavior (Figure S7). In particular, at 2.2 Å distance, we obtain an increase by a factor of 2.6 using a LP energy/pulse frequency of 3.17/3.1 eV.

Strong coupling allows us to tune condition (ii) on demand and reach energetic alignment between optical absorption and HC injection. The ideal realization of a hypothetical system, in which the LSP can be freely tuned to match the pulse frequency, can be estimated by normalizing the injected carriers (at 3.8 eV pulse) by the amount of energy absorbed at each pulse frequency (Figure 3; solid line). The absolute maximum in HE injection for this hypothetical system would be then obtained when the pulse frequency, the LSP resonance, and the efficiency peak are all resonant. As established for our original system in vacuum (Figure 3; black), the real systems will not necessarily feature optimal injection for resonant (pulse vs LSP; circles) drive but perform typically best if driven slightly off-resonantly (triangles). Our proposed optical tuning mechanism via the LP follows the hypothetical efficiency indeed closely down to 3.2 eV. For even larger hybridization, a significant part of the energy is trapped in the cavity subsystem (Figure S6, Figure S7) and is no longer used to generate HCs which results in the under-performance below 3.2 eV.

ATOMISTIC MODEL USING NP DIMERS

One possible atomistic realization of our resonator structure is to simply place a second identical NP close to the NP-molecule system (Figure S1b). LSPRs of the NPs hybridize, resulting in polaritonic eigenstates that resemble those of the generic cavity-NP system. The system is set up such that the gap of the NP dimer is between 9.83 Å (resonance 3.62 eV; see Figure S8) and 4.33 Å (resonance 3.35 eV) and the molecule is placed on the outer side of one of the NPs, so that charge can only be injected from that NP. The driving field is polarized along the axis connecting the NP dimer and CO molecule (z-axis). Normalizing by the increased amount of energy absorbed in this system, the number of injected electrons for this NP dimer system (Figure 3; blue markers) follows again the hypothetical efficiency.

MANIPULATION OF SHAPE

Popular strategies to control the optical properties of NP systems include the manipulation of shape, size, and composition.[53−57] However, such approaches modify the electronic ground state which results in an overall change of optical and catalytic activity.[58] We construct a series of artificially elongated NPs (Figure 3; green markers) by inserting up to 8 atomic layers in the middle of the structure and relaxing the nuclear positions with a simple effective medium theory model (Figure S1c−g; more details in SI). This procedure yields structures with aspect ratios from 1 to 2.14 and ensures that the tail of the NP, where the molecule is positioned, remains a (111) surface in order to be directly comparable to our other results, however the structures differ from conventional nanorods that can be fabricated. The simplistic relaxation results in a minor shift of the LSP injection efficiency even for the 201 Ag NP. Elongating the NPs, and normalizing the injection efficiency by the increase in size, leads to a mild increase in catalytic activity. Changing the shape modifies the ground state and with it the single-particle spectrum, moving the previously observed resonance out of reach. Shape manipulation is clearly a valid alternative but our study illustrates that both approaches feature unique strengths and a holistic optimization strategy that accounts for shape, size, composition, and polaritonic control holds great potential to give birth to a new generation of catalytic materials.

CONCLUSIONS AND OUTLOOK

To summarize, we have illustrated that the efficiency of the direct HC transfer process depends on the alignment of the incoming photon energy, the LSP resonance of the NP, and the excitation energy of a few (or even a single) charge-transfer excitations.[20] We have discussed a polaritonic framework for

https://doi.org/10.1021/acs.nanolett.4c03153
Nano Lett. 2024, 24, 11913−11920

tuning the NP resonance to the charge-transfer excitations based on strong coupling to an electromagnetic resonator structure. In this framework, we achieve a more than 6-fold increase in HC injection with the potential to fine-tune this increase nonintrusively by adjusting the configuration of the resonator. Alternative strategies, based on modifying the NP shape, change LSP and charge-transfer excitations at the same time, resulting in a more complex optimization/control problem. The basic objective of all such techniques remains the same—reaching energetic alignment between optical absorption and injection, thus finding an optimum on the "hypothetical efficiency" curve introduced in Figure 3. Explicitly simulating NP dimers, one possible realization of NP-resonator hybridization, follows indeed closely our simplified cavity model as well as the hypothetical efficiency curve. Notable upsides for the use of electromagnetic resonator structures over the adjustment of shape or composition are 3-fold: (i) A chosen catalyst can be fine-tuned to a specific orbital and thus reaction, allowing for a more modular design-approach. (ii) Some resonator structures can be used to dynamically adjust to changes of the catalyst, appearing, e.g., due to deterioration. (iii) The established approach to boost absorption characteristics, and thus photocatalytic activity, with optical resonators[9,11,21−24] can be conveniently combined with our approach.

Our proposal could be validated in various mixed-plasmonic or collectively coupled systems, many of which are already in striking distance[9,43,59,60] or even exceed[10,42,60] the necessary coupling strength. Minor remaining challenges are the design of resonator structures that have a sufficient quality factor and ensuring that the energy of the field is deposited into the photocatalytic NPs. A promising strategy could be the combination of photocatalytic NPs and dynamically switchable metasurfaces[61] with machine learning supported free-form design.[62] Such a system would be a possible candidate to reach appreciable enantiomer selective catalysis by using a crossover between chiral polaritonics and plasmonics.[63,64] Maxwell-TDDFT approaches, especially those following embedding concepts,[47,51] are ideal to support this task as they provide a computationally accessible framework to consistently link macroscopic optical energy distribution to microscopic HC dynamics. Recall, that direct HC transfer stands in competition with indirect transfer and catalytic increase due to heating[1,65−68]—a competition that is sensitive to various characteristics of the material and selection rules imposed by symmetry of its surface.[69,70] Understanding the delicate HC injection process with the help of the adjustable nonintrusive control-knob discussed here would deepen our understanding of plasmonic catalysis and open new avenues for refined designs that will be required in the near future to elevate the hydrogen economy to the desired level. This includes the connection between energy absorption and chemical reactivity[71,72] as well as the impact of prolonged nonequilibrium carrier distribution (before thermalization to HCs) on the reactivity.

To this end, polaritonically steered plasmonic catalysis might open a path to replace precious materials, such as platinum and gold, with more abundant and optically active materials, such as aluminum,[73] thus triggering the next development step toward green chemistry.

■ ASSOCIATED CONTENT

Data Availability Statement

The data generated in this study are openly available via Zenodo at https://zenodo.org/records/13357330.

Supporting Information

The Supporting Information is available free of charge at https://pubs.acs.org/doi/10.1021/acs.nanolett.4c03153.

Atomic structures, computational details, energy absorbed by the no-cavity system, time-resolved number of hot carriers in total and in the molecule, (projected) density of states, transition contribution map, energetic contributions matter and cavity subsystems, electron injection for different NP-molecule distances, and absorption spectra (PDF)

■ AUTHOR INFORMATION

Corresponding Author

Christian Schäfer − *Department of Physics, Chalmers University of Technology, 412 96 Göteborg, Sweden;* orcid.org/0000-0002-8557-733X; Email: christian.schaefer.physics@gmail.com

Authors

Jakub Fojt − *Department of Physics, Chalmers University of Technology, 412 96 Göteborg, Sweden;* orcid.org/0000-0002-8372-3153

Paul Erhart − *Department of Physics, Chalmers University of Technology, 412 96 Göteborg, Sweden;* orcid.org/0000-0002-2516-6061

Complete contact information is available at: https://pubs.acs.org/10.1021/acs.nanolett.4c03153

Notes

The GPAW package[74,75] with linear combination of atomic orbitals (LCAO) basis sets,[76] LCAO-RT-TDDFT implementation,[77] and radiation-reaction potential[47,51] was used for the RT-TDDFT calculations. The Gritsenko-van Leeuwen-van Lenthe-Baerendssolid-correlation (GLLB-sc)[78,79] XC-functional, utilizing the Libxc[80] library, was used in GPAW. The VASP[81−84] suite with the projector augmented wave[85] method and the vdW-DF-cx[86−89] XC-functional was used for the structure relaxations. The ASE library[90] was used for constructing and manipulating atomic structures. The rhodent package[91] was used for processing results from the RT-TDDFT calculations in order to obtain energies and hot carriers. The NumPy,[92] SciPy,[93] and Matplotlib[94] Python packages were used for processing and plotting data.
The authors declare no competing financial interest.

■ ACKNOWLEDGMENTS

J.F. and P.E. acknowledge funding from the Knut and Alice Wallenberg foundation through Grant No. 2019.0140 and from the Swedish Research Council through Grant No. 2020-04935. C.S. acknowledges funding from the Horizon Europe research and innovation program of the European Union under the Marie Skłodowska-Curie grant agreement no. 101065117. The computations were enabled by resources provided by the National Academic Infrastructure for Supercomputing in Sweden (NAISS) at NSC, PDC, and C3SE partially funded by the Swedish Research Council through grant agreement no. 2022-06725. Partially funded by the European Union. Views and opinions expressed are, however,

those of the author(s) only and do not necessarily reflect those of the European Union or REA. Neither the European Union nor the granting authority can be held responsible for them.

■ ADDITIONAL NOTES

[a]We note that in real-time time-dependent density functional theory (RT-TDDFT) with an adiabatic exchange correlation (XC)-kernel, decay channels such as Auger and phonon scattering are missing and the lifetime is infinite. Since we are simulating a finite pulse with a full-width at half-maximum of 0.7 eV in frequency space, the resonant condition is broadened accordingly.

[b]We use the simplified expression $v_{\mathrm{rr}}(\mathbf{r}, t) = \frac{8\pi}{V}\epsilon_z \cdot \mathbf{r}\partial_l \sin(\omega_c t)/\omega_c e^{-t/\tau}$ (in atomic units). Here, ϵ_z is the polarization of the cavity, V is the effective mode-volume, ω_c is the cavity frequency (set in resonance to the LSPR), and τ is the lifetime of the optical mode which is connected to the quality factor of the cavity.

[c]If the polaritonic states overlap with a broad darkstate distribution, a fraction of the energy deposited in the polaritons will leak into the dark states. That fraction (energy lost to dark states/energy provided) would follow the standard injection probabilities which lowers the fraction of our enhancement.

■ REFERENCES

(1) Zhou, L.; Swearer, D. F.; Zhang, C.; Robatjazi, H.; Zhao, H.; Henderson, L.; Dong, L.; Christopher, P.; Carter, E. A.; Nordlander, P.; Halas, N. J. Quantifying Hot Carrier and Thermal Contributions in Plasmonic Photocatalysis. *Science* **2018**, *362*, 69−72.

(2) Geng, X.; Abdellah, M.; Bericat Vadell, R.; Folkenant, M.; Edvinsson, T.; Sá, J. Direct Plasmonic Solar Cell Efficiency Dependence on Spiro-OMeTAD Li-TFSI Content. *Nanomaterials* **2021**, *11*, 3329.

(3) Aslam, U.; Rao, V. G.; Chavez, S.; Linic, S. Catalytic Conversion of Solar to Chemical Energy on Plasmonic Metal Nanostructures. *Nat. Catal.* **2018**, *1*, 656−665.

(4) Li, R.; Cheng, W.-H.; Richter, M. H.; DuChene, J. S.; Tian, W.; Li, C.; Atwater, H. A. Unassisted Highly Selective Gas-Phase CO2 Reduction with a Plasmonic Au/p-GaN Photocatalyst Using H2O as an Electron Donor. *ACS Energy Lett.* **2021**, *6*, 1849−1856.

(5) DuChene, J. S.; Tagliabue, G.; Welch, A. J.; Cheng, W.-H.; Atwater, H. A. Hot Hole Collection and Photoelectrochemical CO2 Reduction with Plasmonic Au/p-GaN Photocathodes. *Nano Lett.* **2018**, *18*, 2545−2550.

(6) Zhou, L.; Lou, M.; Bao, J. L.; Zhang, C.; Liu, J. G.; Martirez, J. M. P.; Tian, S.; Yuan, L.; Swearer, D. F.; Robatjazi, H.; Carter, E. A.; Nordlander, P.; Halas, N. J. Hot Carrier Multiplication in Plasmonic Photocatalysis. *Proc. Natl. Acad. Sci. U.S.A.* **2021**, *118*, e2022109118.

(7) DuChene, J. S.; Tagliabue, G.; Welch, A. J.; Li, X.; Cheng, W.-H.; Atwater, H. A. Optical Excitation of a Nanoparticle Cu/p-NiO Photocathode Improves Reaction Selectivity for CO2 Reduction in Aqueous Electrolytes. *Nano Lett.* **2020**, *20*, 2348−2358.

(8) Hou, T.; Chen, L.; Xin, Y.; Zhu, W.; Zhang, C.; Zhang, W.; Liang, S.; Wang, L. Porous CuFe for Plasmon-Assisted N2 Photofixation. *ACS Energy Lett.* **2020**, *5*, 2444−2451.

(9) Gupta, V.; Sarkar, S.; Aftenieva, O.; Tsuda, T.; Kumar, L.; Schletz, D.; Schultz, J.; Kiriy, A.; Fery, A.; Vogel, N.; Konig, T. A. F. Nanoimprint Lithography Facilitated Plasmonic-Photonic Coupling for Enhanced Photoconductivity and Photocatalysis. *Adv. Funct. Mater.* **2021**, *31*, 2105054.

(10) Herran, M.; Juergensen, S.; Kessens, M.; Hoeing, D.; Köppen, A.; Sousa-Castillo, A.; Parak, W. J.; Lange, H.; Reich, S.; Schulz, F.; et al. Plasmonic bimetallic two-dimensional supercrystals for H2 generation. *Nature Catalysis* **2023**, *6*, 1205−1214.

(11) Yuan, L.; Zhao, Y.; Toma, A.; Aglieri, V.; Gerislioglu, B.; Yuan, Y.; Lou, M.; Ogundare, A.; Alabastri, A.; Nordlander, P.; Halas, N. J. A Quasi-Bound States in the Continuum Dielectric Metasurface-Based Antenna−Reactor Photocatalyst. *Nano Lett.* **2024**, *24*, 172−179.

(12) Bohren, C. F. How Can a Particle Absorb More than the Light Incident on It? *Am. J. Phys.* **1983**, *51*, 323−327.

(13) Langhammer, C.; Kasemo, B.; Zorić, I. Absorption and Scattering of Light by Pt, Pd, Ag, and Au Nanodisks: Absolute Cross Sections and Branching Ratios. *J. Chem. Phys.* **2007**, *126*, 194702.

(14) Douglas-Gallardo, O. A.; Berdakin, M.; Sánchez, C. G. Atomistic Insights into Chemical Interface Damping of Surface Plasmon Excitations in Silver Nanoclusters. *J. Phys. Chem. C* **2016**, *120*, 24389−24399.

(15) Khurgin, J. B.; Petrov, A.; Eich, M.; Uskov, A. V. Direct Plasmonic Excitation of the Hybridized Surface States in Metal Nanoparticles. *ACS Photonics* **2021**, *8*, 2041−2049.

(16) Linic, S.; Aslam, U.; Boerigter, C.; Morabito, M. Photochemical Transformations on Plasmonic Metal Nanoparticles. *Nat. Mater.* **2015**, *14*, 567−576.

(17) Christopher, P.; Xin, H.; Linic, S. Visible-Light-Enhanced Catalytic Oxidation Reactions on Plasmonic Silver Nanostructures. *Nat. Chem.* **2011**, *3*, 467−472.

(18) Seemala, B.; Therrien, A. J.; Lou, M.; Li, K.; Finzel, J. P.; Qi, J.; Nordlander, P.; Christopher, P. Plasmon-Mediated Catalytic O2 Dissociation on Ag Nanostructures: Hot Electrons or Near Fields? *ACS Energy Lett.* **2019**, *4*, 1803−1809.

(19) Ostovar, B.; Lee, S. A.; Mehmood, A.; Farrell, K.; Searles, E. K.; Bourgeois, B.; Chiang, W.-Y.; Misiura, A.; Gross, N.; Al-Zubeidi, A.; Dionne, J. A.; Landes, C. F.; Zanni, M.; Levine, B. G.; Link, S. The Role of the Plasmon in Interfacial Charge Transfer. *Science Advances* **2024**, *10*, eadp3353.

(20) Fojt, J.; Rossi, T. P.; Kuisma, M.; Erhart, P. Hot-Carrier Transfer across a Nanoparticle−Molecule Junction: The Importance of Orbital Hybridization and Level Alignment. *Nano Lett.* **2022**, *22*, 8786−8792.

(21) Ren, H.; Yang, J.-L.; Yang, W.-M.; Zhong, H.-L.; Lin, J.-S.; Radjenovic, P. M.; Sun, L.; Zhang, H.; Xu, J.; Tian, Z.-Q.; Li, J.-F. Core−Shell−Satellite Plasmonic Photocatalyst for Broad-Spectrum Photocatalytic Water Splitting. *ACS Materials Letters* **2021**, *3*, 69−76.

(22) Jin, H.; Herran, M.; Cortés, E.; Lischner, J. Theory of Hot-Carrier Generation in Bimetallic Plasmonic Catalysts. *ACS Photonics* **2023**, *10*, 3629−3636.

(23) Herran, M.; Juergensen, S.; Kessens, M.; Hoeing, D.; Köppen, A.; Sousa-Castillo, A.; Parak, W. J.; Lange, H.; Reich, S.; Schulz, F.; Cortés, E. Plasmonic Bimetallic Two-Dimensional Supercrystals for H2 Generation. *Nat. Catal.* **2023**, *6*, 1205−1214.

(24) Nan, L.; Giráldez-Martínez, J.; Stefancu, A.; Zhu, L.; Liu, M.; Govorov, A. O.; Besteiro, L. V.; Cortés, E. Investigating Plasmonic Catalysis Kinetics on Hot-Spot Engineered Nanoantennae. *Nano Lett.* **2023**, *23*, 2883−2889.

(25) Feist, J.; Garcia-Vidal, F. J. Extraordinary Exciton Conductance Induced by Strong Coupling. *Phys. Rev. Lett.* **2015**, *114*, 196402.

(26) Xiang, B.; Ribeiro, R. F.; Dunkelberger, A. D.; Wang, J.; Li, Y.; Simpkins, B. S.; Owrutsky, J. C.; Yuen-Zhou, J.; Xiong, W. Two-dimensional infrared spectroscopy of vibrational polaritons. *Proc. Natl. Acad. Sci. U. S. A.* **2018**, *115*, 4845.

(27) Du, M.; Martínez-Martínez, L. A.; Ribeiro, R. F.; Hu, Z.; Menon, V. M.; Yuen-Zhou, J. Theory for polariton-assisted remote energy transfer. *Chemical science* **2018**, *9*, 6659−6669.

(28) Groenhof, G.; Climent, C.; Feist, J.; Morozov, D.; Toppari, J. J. Tracking Polariton Relaxation with Multiscale Molecular Dynamics Simulations. *journal of physical chemistry letters* **2019**, *10*, 5476−5483.

(29) de Jong, L. M. A.; Berghuis, A. M.; Abdelkhalik, M. S.; van der Pol, T. P. A.; Wienk, M. M.; Janssen, R. A. J.; Gomez Rivas, J. Enhancement of the internal quantum efficiency in strongly coupled P3HT-C60 organic photovoltaic cells using Fabry−Perot cavities with varied cavity confinement. *Nanophotonics* **2024**, *13*, 2531−2540.

https://doi.org/10.1021/acs.nanolett.4c03153
Nano Lett. 2024, 24, 11913−11920

(30) Orgiu, E.; George, J.; Hutchison, J. A.; Devaux, E.; Dayen, J. F.; Doudin, B.; Stellacci, F.; Genet, C.; Schachenmayer, J.; Genes, C.; Pupillo, G.; Samorì, P.; Ebbesen, T. W. Conductivity in organic semiconductors hybridized with the vacuum field. *Nat. Mater.* **2015**, *14*, 1123−1129.
(31) Herrera, F.; Spano, F. C. Cavity-Controlled Chemistry in Molecular Ensembles. *Phys. Rev. Lett.* **2016**, *116*, 238301.
(32) Schäfer, C.; Ruggenthaler, M.; Appel, H.; Rubio, A. Modification of excitation and charge transfer in cavity quantum-electrodynamical chemistry. *Proc. Natl. Acad. Sci. U. S. A.* **2019**, *116*, 4883−4892.
(33) Kumar, S.; Biswas, S.; Rashid, U.; Mony, K. S.; Chandrasekharan, G.; Mattiotti, F.; Vergauwe, R. M. A.; Hagenmuller, D.; Kaliginedi, V.; Thomas, A. Extraordinary Electrical Conductance through Amorphous Nonconducting Polymers under Vibrational Strong Coupling. *Journal of the American Chemical Society* **2024**, *146*, 18999.
(34) Hutchison, J. A.; Schwartz, T.; Genet, C.; Devaux, E.; Ebbesen, T. W. Modifying Chemical Landscapes by Coupling to Vacuum Fields. *Angew. Chem., Int. Ed.* **2012**, *51*, 1592−1596.
(35) Munkhbat, B.; Wersäll, M.; Baranov, D. G.; Antosiewicz, T. J.; Shegai, T. Suppression of photo-oxidation of organic chromophores by strong coupling to plasmonic nanoantennas. *Science Advances* **2018**, *4*, eaas9552.
(36) Ahn, W.; Triana, J. F.; Recabal, F.; Herrera, F.; Simpkins, B. S. Modification of ground-state chemical reactivity via light−matter coherence in infrared cavities. *Science* **2023**, *380*, 1165−1168.
(37) Chen, T.-T.; Du, M.; Yang, Z.; Yuen-Zhou, J.; Xiong, W. Cavity-enabled enhancement of ultrafast intramolecular vibrational redistribution over pseudorotation. *Science* **2022**, *378*, 790−794.
(38) Galego, J.; Garcia-Vidal, F. J.; Feist, J. Suppressing photochemical reactions with quantized light fields. *Nat. Commun.* **2016**, *7*, 13841.
(39) Fregoni, J.; Granucci, G.; Persico, M.; Corni, S. Strong coupling with light enhances the photoisomerization quantum yield of azobenzene. *Chem.* **2020**, *6*, 250−265.
(40) Schäfer, C.; Flick, J.; Ronca, E.; Narang, P.; Rubio, A. Shining light on the microscopic resonant mechanism responsible for cavity-mediated chemical reactivity. *Nat. Commun.* **2022**, *13*, 7817.
(41) Schäfer, C.; Fojt, J.; Lindgren, E.; Erhart, P. Machine Learning for Polaritonic Chemistry: Accessing Chemical Kinetics. *J. Am. Chem. Soc.* **2024**, *146*, 5402−5413.
(42) Mueller, N. S.; Okamura, Y.; Vieira, B. G.; Juergensen, S.; Lange, H.; Barros, E. B.; Schulz, F.; Reich, S. Deep strong light−matter coupling in plasmonic nanoparticle crystals. *Nature* **2020**, *583*, 780−784.
(43) Hertzog, M.; Munkhbat, B.; Baranov, D.; Shegai, T.; Börjesson, K. Enhancing Vibrational Light−Matter Coupling Strength beyond the Molecular Concentration Limit Using Plasmonic Arrays. *Nano Lett.* **2021**, *21*, 1320−1326.
(44) Kluczyk-Korch, K.; Antosiewicz, T. J. Hot carrier generation in a strongly coupled molecule−plasmonic nanoparticle system. *Nanophotonics* **2023**, *12*, 1711−1722.
(45) Rossi, T. P.; Kuisma, M.; Puska, M. J.; Nieminen, R. M.; Erhart, P. Kohn−Sham Decomposition in Real-Time Time-Dependent Density-Functional Theory: An Efficient Tool for Analyzing Plasmonic Excitations. *J. Chem. Theory Comput.* **2017**, *13*, 4779−4790.
(46) Rossi, T. P.; Erhart, P.; Kuisma, M. Hot-Carrier Generation in Plasmonic Nanoparticles: The Importance of Atomic Structure. *ACS Nano* **2020**, *14*, 9963−9971.
(47) Schäfer, C.; Johansson, G. Shortcut to Self-Consistent Light-Matter Interaction and Realistic Spectra from First Principles. *Phys. Rev. Lett.* **2022**, *128*, 156402.
(48) Manjavacas, A.; Liu, J. G.; Kulkarni, V.; Nordlander, P. Plasmon-Induced Hot Carriers in Metallic Nanoparticles. *ACS Nano* **2014**, *8*, 7630−7638.
(49) Kaniber, M.; Schraml, K.; Regler, A.; Bartl, J.; Glashagen, G.; Flassig, F.; Wierzbowski, J.; Finley, J. J. Surface Plasmon Resonance Spectroscopy of Single Bowtie Nano-Antennas Using a Differential Reflectivity Method. *Sci. Rep.* **2016**, *6*, 23203.
(50) Baumberg, J. J.; Aizpurua, J.; Mikkelsen, M. H.; Smith, D. R. Extreme Nanophotonics from Ultrathin Metallic Gaps. *Nat. Mater.* **2019**, *18*, 668−678.
(51) Schäfer, C. Polaritonic Chemistry from First Principles via Embedding Radiation Reaction. *J. Phys. Chem. Lett.* **2022**, *13*, 6905−6911.
(52) Schäfer, C.; Ruggenthaler, M.; Rokaj, V.; Rubio, A. Relevance of the quadratic diamagnetic and self-polarization terms in cavity quantum electrodynamics. *ACS photonics* **2020**, *7*, 975−990.
(53) Slaughter, L. S.; Chang, W.-S.; Swanglap, P.; Tcherniak, A.; Khanal, B. P.; Zubarev, E. R.; Link, S. Single-Particle Spectroscopy of Gold Nanorods beyond the Quasi-Static Limit: Varying the Width at Constant Aspect Ratio. *J. Phys. Chem. C* **2010**, *114*, 4934−4938.
(54) Xiang, H.; Wang, Z.; Xu, L.; Zhang, X.; Lu, G. Quantum Plasmonics in Nanorods: A Time-Dependent Orbital-Free Density Functional Theory Study with Thousands of Atoms. *J. Phys. Chem. C* **2020**, *124*, 945−951.
(55) Kim, S.; Huynh, L. T. M.; Yoon, S. Which Nanoparticle Shape Is the Most Effective in Generating Hot Charge Carriers from Plasmon Excitation? *J. Phys. Chem. C* **2023**, *127*, 14776−14783.
(56) Renard, D.; Tian, S.; Lou, M.; Neumann, O.; Yang, J.; Bayles, A.; Solti, D.; Nordlander, P.; Halas, N. J. UV-Resonant Al Nanocrystals: Synthesis, Silica Coating, and Broadband Photothermal Response. *Nano Lett.* **2021**, *21*, 536−542.
(57) Fojt, J.; Rossi, T. P.; Kumar, P. V.; Erhart, P. Tailoring Hot-Carrier Distributions of Plasmonic Nanostructures through Surface Alloying. *ACS Nano* **2024**, *18*, 6398−6405.
(58) Jin, H.; Kahk, J. M.; Papaconstantopoulos, D. A.; Ferreira, A.; Lischner, J. Plasmon-Induced Hot Carriers from Interband and Intraband Transitions in Large Noble Metal Nanoparticles. *PRX Energy* **2022**, *1*, 013006.
(59) Sarkar, S.; Gupta, V.; Kumar, M.; Schubert, J.; Probst, P. T.; Joseph, J.; König, T. A. Hybridized Guided-Mode Resonances via Colloidal Plasmonic Self-Assembled Grating. *ACS Appl. Mater. Interfaces* **2019**, *11*, 13752−13760.
(60) Baumberg, J. J.; Aizpurua, J.; Mikkelsen, M. H.; Smith, D. R. Extreme nanophotonics from ultrathin metallic gaps. *Nature materials* **2019**, *18*, 668−678.
(61) Maiuri, M.; Schirato, A.; Cerullo, G.; Della Valle, G. Ultrafast All-Optical Metasurfaces: Challenges and New Frontiers. *ACS Photonics* **2024**, *11*, 2888−2905.
(62) Gahlmann, T.; Tassin, P. Deep neural networks for the prediction of the optical properties and the free-form inverse design of metamaterials. *Phys. Rev. B* **2022**, *106*, 085408.
(63) Schäfer, C.; Baranov, D. G. Chiral Polaritonics: Analytical Solutions, Intuition, and Use. *J. Phys. Chem. Lett.* **2023**, *14*, 3777−3784.
(64) Baranov, D. G.; Schäfer, C.; Gorkunov, M. V. Toward Molecular Chiral Polaritons. *ACS Photonics* **2023**, *10*, 2440−2455.
(65) Dubi, Y.; Un, I. W.; Sivan, Y. Thermal Effects − an Alternative Mechanism for Plasmon-Assisted Photocatalysis. *Chem. Sci.* **2020**, *11*, 5017−5027.
(66) Jain, P. K. Comment on "Thermal Effects − an Alternative Mechanism for Plasmon-Assisted Photocatalysis" by Y. Dubi, I. W. Un and Y. Sivan, Chem. Sci., 2020, 11, 5017. *Chem. Sci.* **2020**, *11*, 9022−9023.
(67) Sivan, Y.; Baraban, J.; Un, I. W.; Dubi, Y. Comment on "Quantifying Hot Carrier and Thermal Contributions in Plasmonic Photocatalysis. *Science* **2019**, *364*, eaaw9367.
(68) Zhou, L.; Swearer, D. F.; Robatjazi, H.; Alabastri, A.; Christopher, P.; Carter, E. A.; Nordlander, P.; Halas, N. J. Response to Comment on "Quantifying Hot Carrier and Thermal Contributions in Plasmonic Photocatalysis. *Science* **2019**, *364*, eaaw9545.
(69) Gumhalter, B.; Petek, H. Interplay of electron-photon and electron-plasmon interactions at surfaces: Photonics and plasmonics in juxtaposition. *Prog. Surf. Sci.* **2023**, *98*, 100708.

https://doi.org/10.1021/acs.nanolett.4c03153
Nano Lett. 2024, 24, 11913−11920

(70) Novko, D.; Despoja, V.; Reutzel, M.; Li, A.; Petek, H.; Gumhalter, B. Plasmonically assisted channels of photoemission from metals. *Phys. Rev. B* **2021**, *103*, 205401.
(71) Dall'Osto, G.; Marsili, M.; Vanzan, M.; Toffoli, D.; Stener, M.; Corni, S.; Coccia, E. Peeking into the Femtosecond Hot-Carrier Dynamics Reveals Unexpected Mechanisms in Plasmonic Photocatalysis. *J. Am. Chem. Soc.* **2024**, *146*, 2208−2218.
(72) Gardner, J.; Habershon, S.; Maurer, R. J. Assessing mixed quantum-classical molecular dynamics methods for nonadiabatic dynamics of molecules on metal surfaces. *J. Phys. Chem. C* **2023**, *127*, 15257−15270.
(73) Yuan, L.; Kuriakose, A.; Zhou, J.; Robatjazi, H.; Nordlander, P.; Halas, N. J. Plasmonically Enhanced Hydrogen Evolution with an Al−TiO2-Based Photoelectrode. *J. Phys. Chem. C* **2022**, *126*, 13714−13719.
(74) Mortensen, J. J.; Hansen, L. B.; Jacobsen, K. W. Real-Space Grid Implementation of the Projector Augmented Wave Method. *Phys. Rev. B* **2005**, *71*, 035109.
(75) Mortensen, J. J.; Larsen, A. H.; Kuisma, M.; Ivanov, A. V.; Taghizadeh, A.; Peterson, A.; Haldar, A.; Dohn, A. O.; Schafer, C.; Jonsson, E. O.; Hermes, E. D.; Nilsson, F. A.; Kastlunger, G.; Levi, G.; Jonsson, H.; Hakkinen, H.; Fojt, J.; Kangsabanik, J.; Sødequist, J.; Lehtomaki, J.; Heske, J.; Enkovaara, J.; Winther, K. T.øs.; Dulak, M.; Melander, M. M.; Ovesen, M.; Louhivuori, M.; Walter, M.; Gjerding, M.; Lopez-Acevedo, O.; Erhart, P.; Warmbier, R.; Wurdemann, R.; Kaappa, S.; Latini, S.; Boland, T. M.; Bligaard, T.; Skovhus, T.ør.; Susi, T.; Maxson, T.; Rossi, T.; Chen, X.; Schmerwitz, Y. L. A.; Schiøtz, J.; Olsen, T.; Jacobsen, K. W.; Thygesen, K. S.; et al. GPAW: An Open Python Package for Electronic Structure Calculations. *J. Chem. Phys.* **2024**, *160*, 092503.
(76) Larsen, A. H.; Vanin, M.; Mortensen, J. J.; Thygesen, K. S.; Jacobsen, K. W. Localized Atomic Basis Set in the Projector Augmented Wave Method. *Phys. Rev. B* **2009**, *80*, 195112.
(77) Kuisma, M.; Sakko, A.; Rossi, T. P.; Larsen, A. H.; Enkovaara, J.; Lehtovaara, L.; Rantala, T. T. Localized Surface Plasmon Resonance in Silver Nanoparticles: Atomistic First-Principles Time-Dependent Density-Functional Theory Calculations. *Phys. Rev. B* **2015**, *91*, 115431.
(78) Gritsenko, O.; van Leeuwen, R.; van Lenthe, E.; Baerends, E. J. Self-Consistent Approximation to the Kohn-Sham Exchange Potential. *Phys. Rev. A* **1995**, *51*, 1944.
(79) Kuisma, M.; Ojanen, J.; Enkovaara, J.; Rantala, T. T. Kohn-Sham Potential with Discontinuity for Band Gap Materials. *Phys. Rev. B* **2010**, *82*, 115106.
(80) Lehtola, S.; Steigemann, C.; Oliveira, M. J. T.; Marques, M. A. L. Recent Developments in Libxc — A Comprehensive Library of Functionals for Density Functional Theory. *SoftwareX* **2018**, *7*, 1−5.
(81) Kresse, G.; Hafner, J. Ab Initio Molecular Dynamics for Liquid Metals. *Phys. Rev. B* **1993**, *47*, 558−561.
(82) Kresse, G.; Furthmüller, J. Efficient Iterative Schemes for Ab Initio Total-Energy Calculations Using a Plane-Wave Basis Set. *Phys. Rev. B* **1996**, *54*, 11169−11186.
(83) Kresse, G.; Furthmüller, J. Efficiency of Ab-Initio Total Energy Calculations for Metals and Semiconductors Using a Plane-Wave Basis Set. *Nato. Sc. S. Ss. Iii. C. S.* **1996**, *6*, 15−50.
(84) Kresse, G.; Joubert, D. From Ultrasoft Pseudopotentials to the Projector Augmented-Wave Method. *Phys. Rev. B* **1999**, *59*, 1758−1775.
(85) Blöchl, P. E. Projector Augmented-Wave Method. *Phys. Rev. B* **1994**, *50*, 17953−17979.
(86) Berland, K.; Hyldgaard, P. Exchange Functional That Tests the Robustness of the Plasmon Description of the van Der Waals Density Functional. *Phys. Rev. B* **2014**, *89*, 035412.
(87) Klimeš, J.; Bowler, D. R.; Michaelides, A. Chemical Accuracy for the van Der Waals Density Functional. *J. Phys.: Condens. Matter* **2010**, *22*, 022201.
(88) Klimeš, J.; Bowler, D. R.; Michaelides, A. Van Der Waals Density Functionals Applied to Solids. *Phys. Rev. B* **2011**, *83*, 195131.
(89) Román-Pérez, G.; Soler, J. M. Efficient Implementation of a van Der Waals Density Functional: Application to Double-Wall Carbon Nanotubes. *Phys. Rev. Lett.* **2009**, *103*, 096102.
(90) Hjorth Larsen, A.; Jørgen Mortensen, J.; Blomqvist, J.; Castelli, I. E; Christensen, R.; Dułak, M.; Friis, J.; Groves, M. N; Hammer, B.ør.; Hargus, C.; Hermes, E. D; Jennings, P. C; Bjerre Jensen, P.; Kermode, J.; Kitchin, J. R; Leonhard Kolsbjerg, E.; Kubal, J.; Kaasbjerg, K.; Lysgaard, S.; Bergmann Maronsson, J.; Maxson, T.; Olsen, T.; Pastewka, L.; Peterson, A.; Rostgaard, C.; Schiøtz, J.; Schutt, O.; Strange, M.; Thygesen, K. S; Vegge, T.; Vilhelmsen, L.; Walter, M.; Zeng, Z.; Jacobsen, K. W; et al. The Atomic Simulation Environment—a Python Library for Working with Atoms. *J. Phys.: Condens. Matter* **2017**, *29*, 273002.
(91) Fojt, J.; Rossi, T.; Erhart, P. *rhodent − Analyzing hot-carrier distributions from TD-DFT simulations*, 2024. https://zenodo.org/records/13332635 (accessed 2024−09−07).
(92) Harris, C. R.; et al. Array Programming with NumPy. *Nature* **2020**, *585*, 357−362.
(93) Virtanen, P.; et al. SciPy 1.0: Fundamental Algorithms for Scientific Computing in Python. *Nat. Methods* **2020**, *17*, 261−272.
(94) Hunter, J. D. Matplotlib: A 2D Graphics Environment. *Comput. Sci. Eng.* **2007**, *9*, 90−95.

https://doi.org/10.1021/acs.nanolett.4c03153
Nano Lett. 2024, 24, 11913−11920

Supplementary Information: Controlling Plasmonic Catalysis via Strong Coupling with Electromagnetic Resonators

Jakub Fojt,[1] Paul Erhart,[1] and Christian Schäfer[1,*]

[1] *Department of Physics, Chalmers University of Technology, 412 96 Göteborg, Sweden*

(Dated: September 10, 2024)

CONTENTS

* Electronic address: christian.schaefer.physics@gmail.com

SUPPLEMENTARY FIGURES

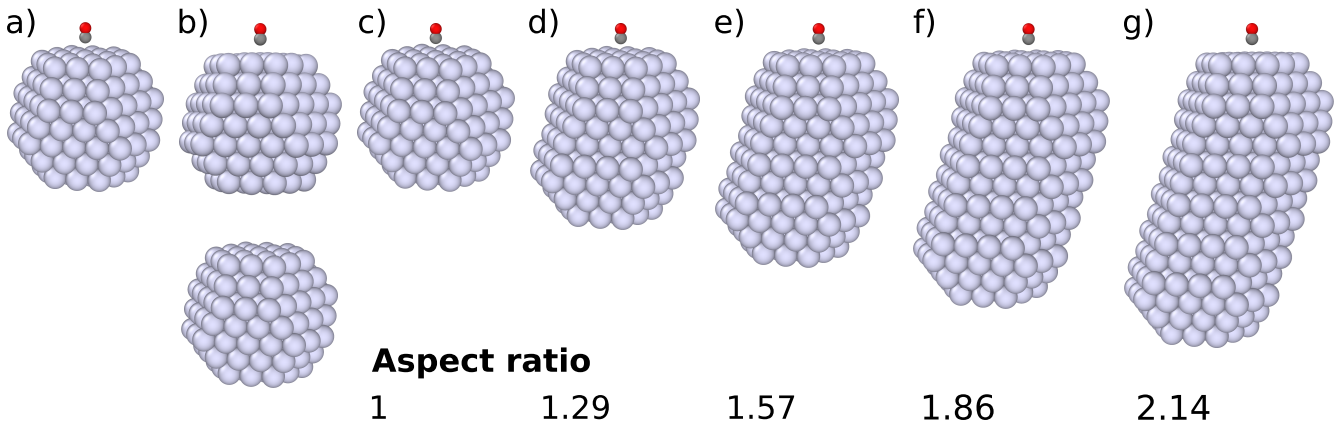

Figure S1. **Atomic structures.** (a) The regular-truncated-octahedron shaped NP with one CO molecule. (b) The NP dimer with the CO molecule placed near one of the NPs. (c-g) A series of elongated NPs with the CO molecule. The elongated structures have been constructed in such a way that the top and bottom (from the point of view of the figure) of the structures are {111} surfaces. The placement of the CO molecule is identical in all structures (a)-(g), centered on the (111) face with its bond axis perpendicular to the surface. In the RT-TDDFT calculations the polarization of the applied field is directed along the bond axis.

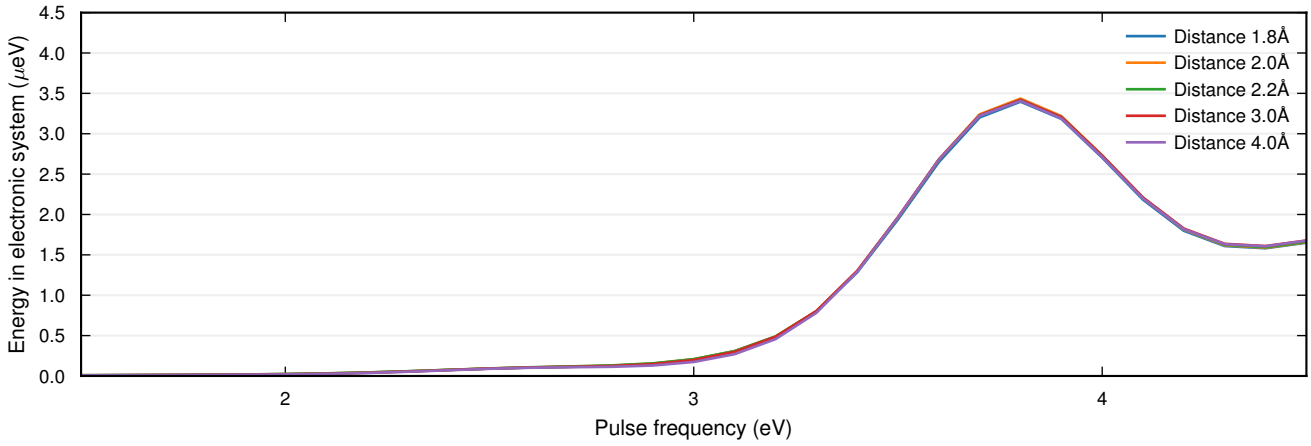

Figure S2. **Amount of energy in the no-cavity system.** Evaluated at the end of the simulation and plotted by pulse frequency. The position of the CO molecule barely makes a difference to the amount of energy absorbed in total.

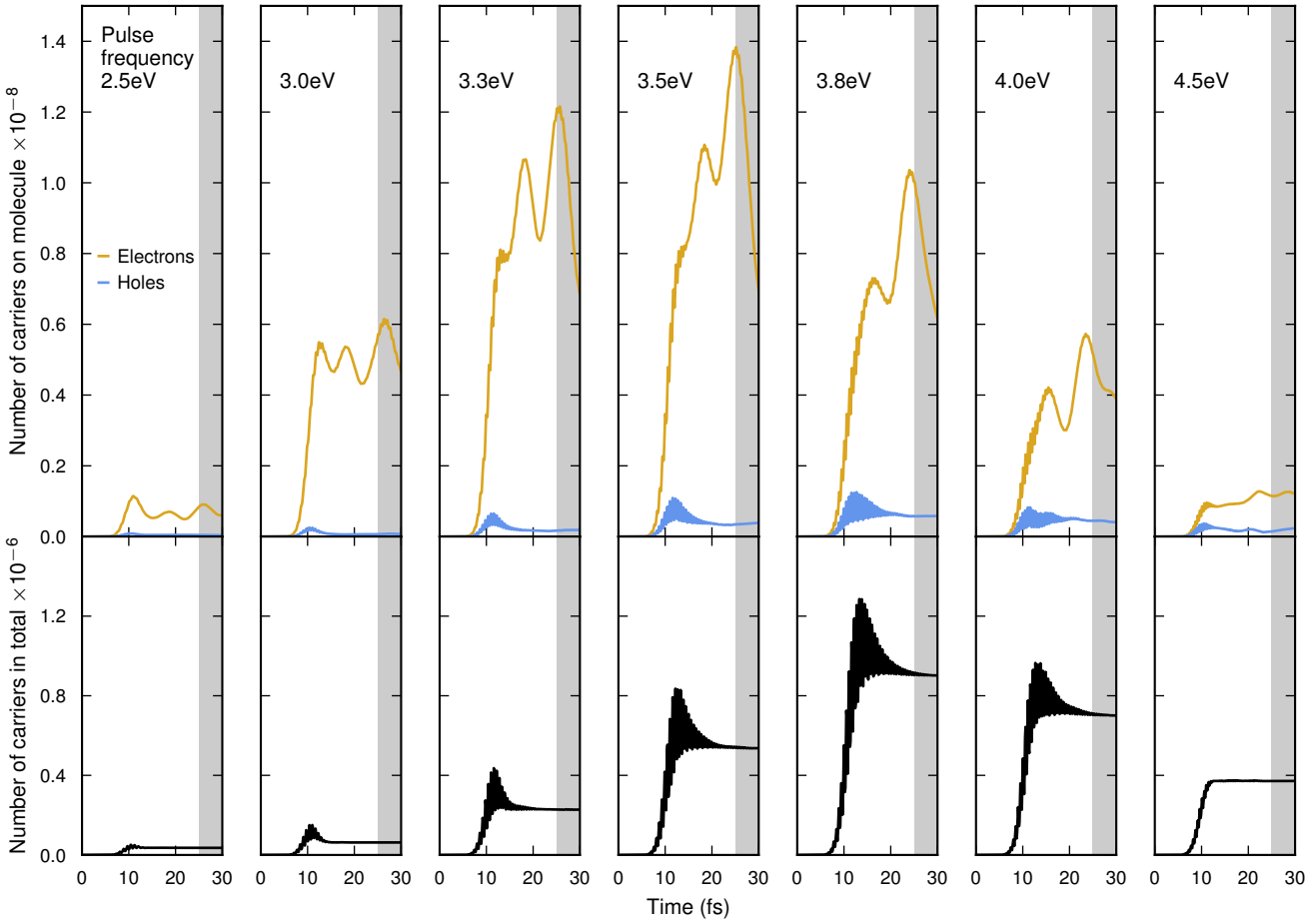

Figure S3. **Hot-carrier generation over time.** For the $3\,\text{Å}$ distance no-cavity system. The number of carriers increases as the plasmon dephases around the $10\,\text{fs}$ mark. While the total number of carriers reaches a steady value towards the end of the simulation, the number of electrons and holes in the molecule fluctuates. At any given time the number of electrons in the molecule is roughly a factor 10-100 smaller than the total number of carriers, and the number of holes in the molecule is a roughly a factor 5-10 smaller than the number of electrons in the molecule. The grey areas mark the time window where an average number of carriers was computed.

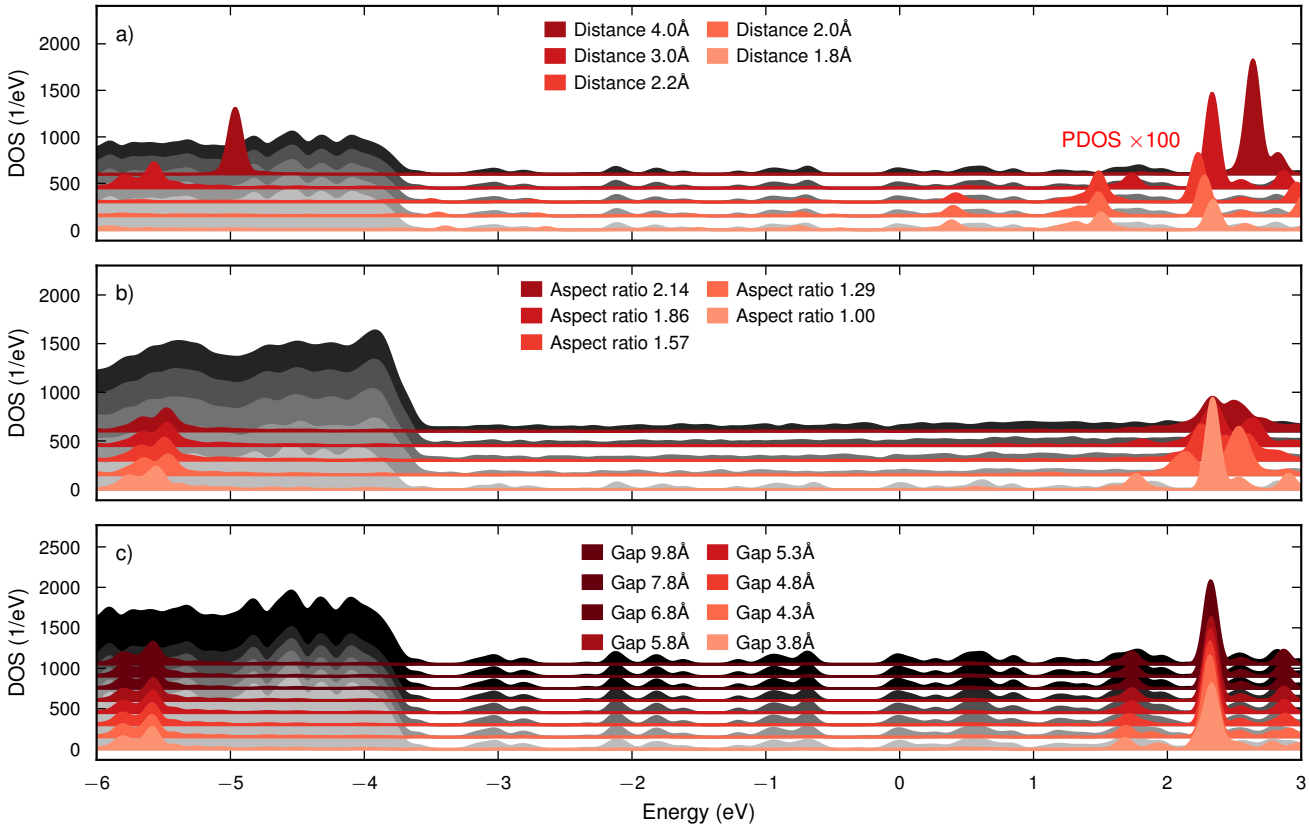

Figure S4. **Density of states and projected density of states of the molecule.** (a) For the NP-molecule system at various distances, (b) for the distance of $3\,\text{Å}$ between the molecule and elongated NPs, and (c) for the two NP, one molecule systems. For distances closer than $3\,\text{Å}$ the molecule is strongly hybridized with the NP, splitting the original LUMO state into many. Elongating the NP by adding several atomic layers to it also affects the hybridization, despite the molecule being kept at the same distance from the surface. Varying the gap in the NP dimer keeps the ground state unchanged, except for at the very smallest gaps, where tiny shifts in the DOS and PDOS are visible. Because the HOMO state is $5\,\text{eV}$ below the Fermi level at large distances, hole transfer to the molecule is virtually impossible. At smaller distances, hybridized branches of the HOMO appear closer to the Fermi level making hole transfer possible, but less prevalent than electron transfer.

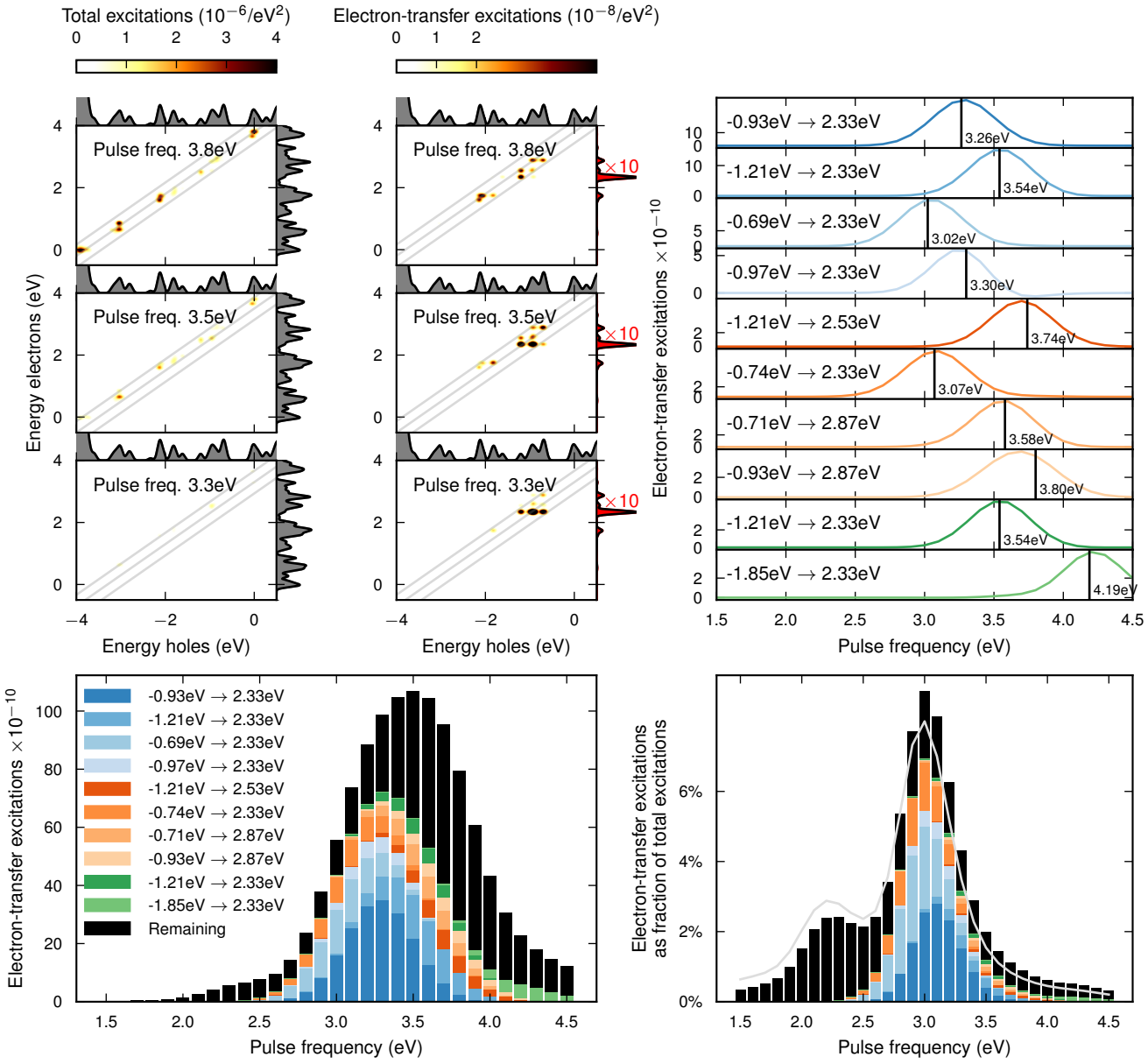

Figure S5. **Transition contribution map for the $3\,\text{Å}$ distance, no cavity case.**
(Top left) The contribution map to total excitations (NP and molecule), as well as projected on the molecule are shown after excitation with three different pulse frequencies.
(Top right) The 10 strongest electron-transfer excitations (that is contribution to the projected transition contribution map) for all pulses between $1.5\,\text{eV}$ and $4.5\,\text{eV}$ are shown. Transitions between degenerate states have been summed and plotted together. The strongest transition is one from the $-0.93\,\text{eV}$ NP state to the $2.33\,\text{eV}$ molecular state, which contributes the most to the number of electrons transferred when the pulse frequency is resonant with the transition energy of $3.26\,\text{eV}$.
(Bottom left) Alternative visualization of the 10 strongest excitations in the top right panel. For each pulse frequency, the amount of each excitation is stacked in color-coded bars, in front of a black bar that represents the total number of electron-transfer excitations (i.e. the data in Fig. 3 in the main text). This shows that at a pulse frequency of $3.2\,\text{eV}$, the $-0.93 \to 2.33\,\text{eV}$ excitation makes up $40\,\%$ all electron-transfer excitations. The 10 strongest excitations add up to almost $80\,\%$ of all electron-transfer excitations. At larger pulse frequencies, those excitations contribute less to electron-transfer because they are further away from their alignment (NP-DOS to LUMO) criterion.
(Bottom right) Same as bottom left, but the values have been divided by the number of HCs generated in total, showing that electron-transfer excitations make up about $7\,\%$ of all HCs when using a pulse frequency of $3\,\text{eV}$. This quantity is closely related to the "hypothetical efficiency" of figure 3 in the main text (which is number of electrons transferred divided by amount of energy absorbed; plotted as a grey line).

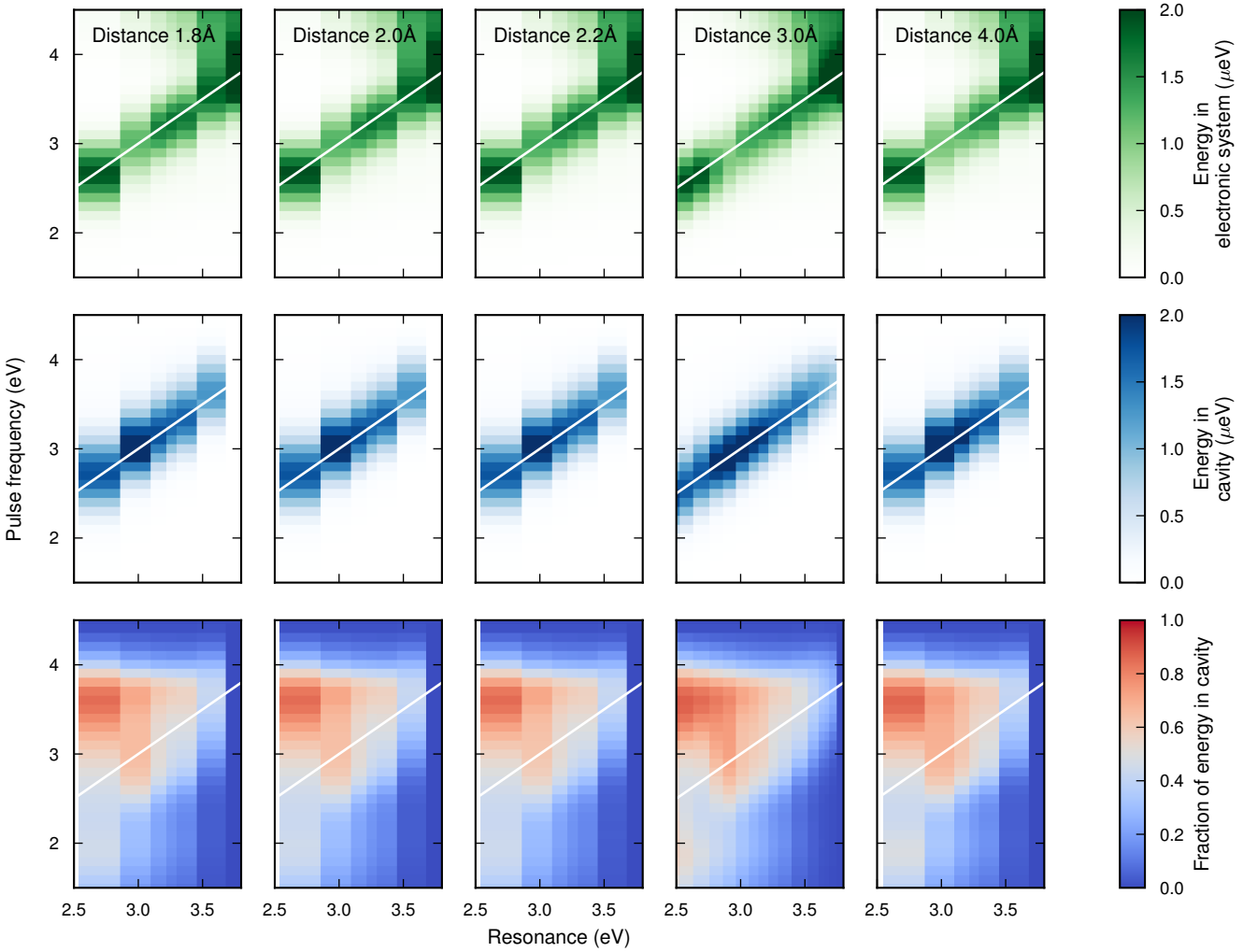

Figure S6. **Amount of energy in the electronic and cavity subsystems.** The energy supplied by the pulse is at the end of the simulation partially in the electronic subsystem and partially in the cavity subsystem. In the case that the resonance is redshifted away from the bare cavity resonance at $3.8\,\mathrm{eV}$, pulses resonant with the bare cavity tend to put a larger fraction into the cavity. Pulses above the d-band edge tend to put a larger fraction of energy into the electronic system.

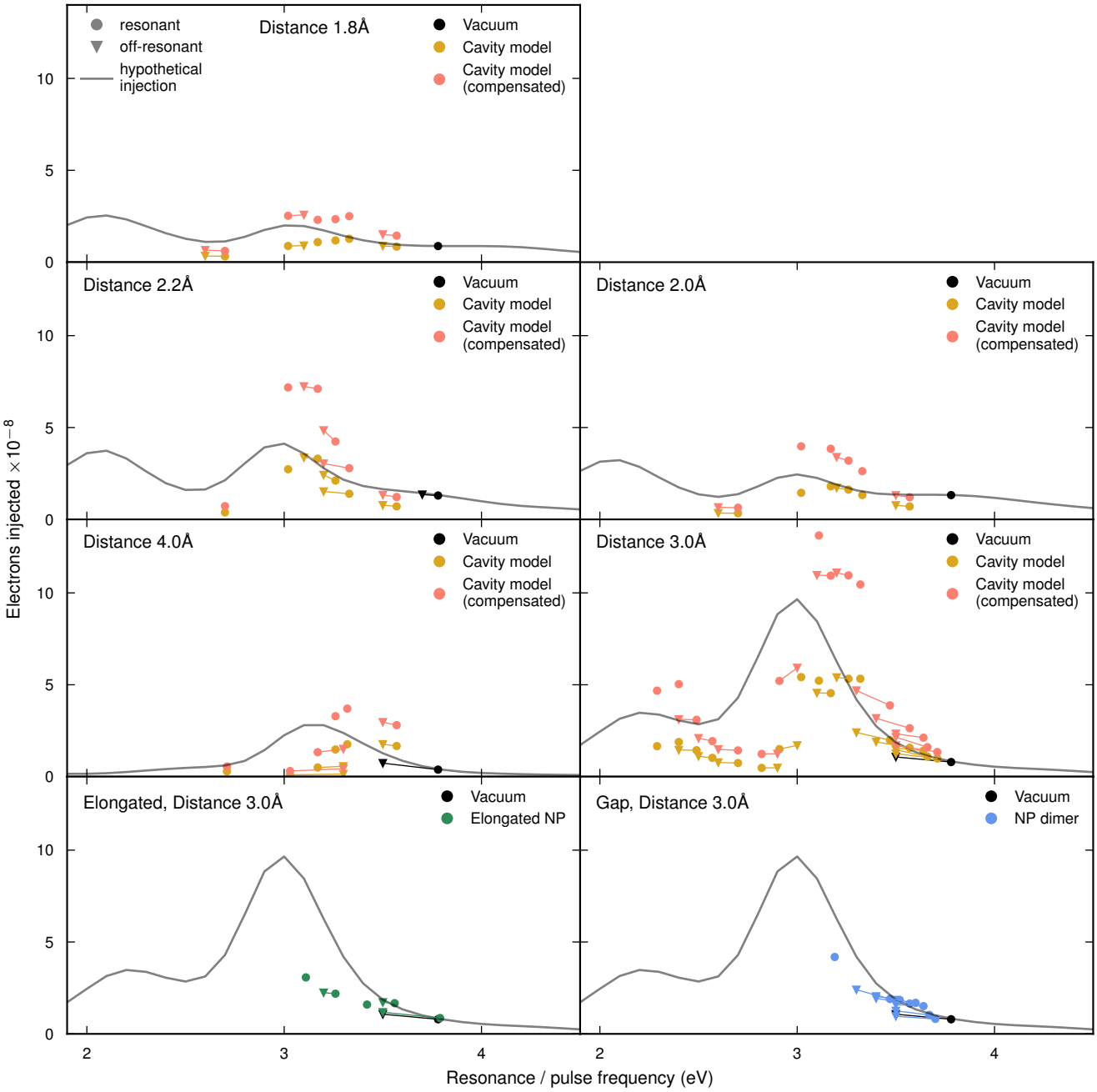

Figure S7. **Number of electrons injected for all considered systems.** Collection of results for different NP-molecule distances, elongated NPs, and NP dimers presented consistent with Fig. 3 of the main manuscript. Elongated and NP dimer efficiencies are normalized such that the same amount of energy is absorbed (see main manuscript) to ensure a fair comparison. As detailed in Fig. S6 and mentioned in the main manuscript, the cavity acts as as energy deposit such that only a fraction of the absorbed energy can be used to generate HCs. Compensating for this 'lost' energy by scaling the efficiency by the energy missing in the matter system ("Cavity model (compensated)"; orange) pushes the efficiency even beyond the hypothetical curve. This suggests that the LSP changes its character when strongly coupled to the cavity, emphasizing the need for reliable theoretical investigations that go beyond optimization based on the simplistic hypothetical curve. Very small distances between the NP dimers results in strong hybridization which in turn strongly modifies the LSP (see Fig. S8) and leads to the outlier at 2.6 eV resonance energy.

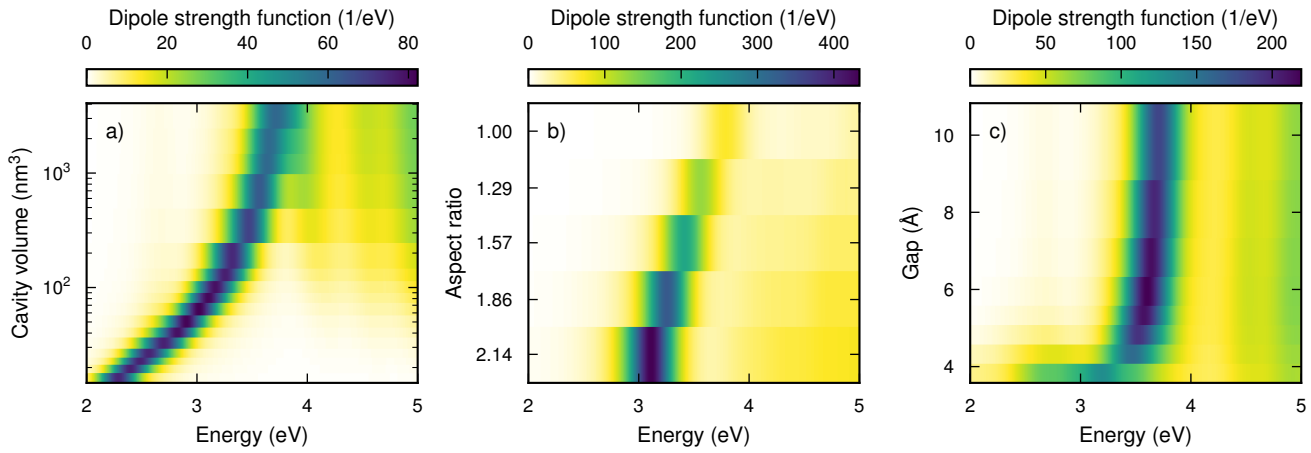

Figure S8. **Absorption spectra.** (a) For the $3\,\text{Å}$ distance system in an optical cavity. The coupling strength to the cavity is inversely proportional to the cavity volume. (b) For the NPs which have been elongated by inserting atomic layers in the middle. As the number of atomic layers is added, the number of electrons in the system, and thus total absorption increases. (c) For the NP dimer. For the smallest gap, the spectrum is drastically broadened.

SUPPLEMENTARY METHODS

Atomic structures

The atomic structure for the 201-atom Ag NP was taken from from Ref. 1. This NP has the shape of a regular truncated octahedron. In Ref. 1, the NP was relaxed with VASP [2–4] using a plane-wave basis set, the PAW [5, 6] method, the vdW-df-cx [7–10] XC-functional, a plane wave cutoff 500 eV, and Gaussian occupation number smearing scheme with the parameter 0.1 eV. Structure relaxations were performed using the conjugate gradient relaxation method implemented in VASP. Relaxation was stopped when the maximal force on any atom fell below $0.015\,\mathrm{eV\,Å^{-1}}$.

For the analysis in the main text, we place a CO molecule with the bond length 1.144 Å at a distance of 3 Å from the center atom of the (111) face of the NP. The molecule is oriented with the C atom towards the surface, and the bond axis perpendicular to the surface (Fig. S1a). The polarization of the applied field in the TDDFT simulation is chosen along the bond axis. After constructing the NP+molecule structure, it *is not* relaxed further, in order to study the charge transfer at a fixed distance. In the SI, we also present results using structures where the distances are 1.8, 2.0, 2.4 and 4 Å.

For the analysis in the main text, we construct a NP dimer by duplicating the NP and shifting it a distance along the bond axis of the molecule. The CO molecule is added at a distance of 3 Å in the same configuration as before, in such a way that it is on the outer side of the NP dimer (Fig. S1b). We shift the NP so the center-center distance is between 24 and 18.5 Å, corresponding to an edge-to-edge distance of between 9.83 and 4.33 Å. In the SI, we also present an additional data point where the center-center distance is 18 Å and the edge-to-edge distance 3.83 Å.

For the analysis in the main text, we construct a series of artificially elongated NPs, by splitting the NP in the middle, shifting the structures apart to make room for two new layers, and duplicating the two atomic layers in the middle of the NP and placing them in the gap. To preserve the surfaces of the NP, the shifted half also has to be shifted laterally, in order to create a tilted structure. This is repeated between 0 and 4 times to create structures with between 0 and 8 added layers, corresponding to aspect ratios of between 1 and 2.14 (Fig. S1c-g). Here, we define the aspect ratio to be the ratio between the smallest number of atomic layers between two opposing {111} faces (which is always 7) and the largest number of atomic layers between two opposing {111} faces (which is 7 plus the number of added layers). These structures are relaxed with the EMT method and BFGS optimizer implemented in ASE [11] until the maximal force is $0.001\,\mathrm{eV\,Å^{-1}}$.

Computational details

We carried out DFT and real-time TDDFT calculations using the GPAW package [12, 13] with LCAO basis sets [14], LCAO-RTTDDFT implementation [15], and the ASE library [11].

For the computation of the ground state we used the GLLB-SC [16, 17] XC-functional, utilizing the Libxc [18] library. We used the *pvalence* [15] basis set for Ag, which is optimized to represent bound unoccupied states, and the dzp basis set for CO. The structures were padded with at least 6 Å of vacuum, and we used a grid spacing of 0.2 Å for wave functions and 0.1 Å for potentials. The Coulomb potential was represented in numerical form on the grid, with an additional analytic moment correction [19] centered at the NP. Fermi-Dirac occupation number smearing with width 0.05 eV was used. The self-consistent loop was stopped when the integral of the difference between two subsequent densities was less than 1×10^{-12}. Pulay [20]-mixing was used to accelerate the ground state convergence.

We applied a δ-kick [21] of strength 10^{-5} in atomic units, and performed time propagation in steps of 10 as for a total length of 30 fs using the adiabatic GLLB-SC kernel. The Fourier transform of the Kohn-Sham density matrix was built up on the fly during propagation and saved on a predefined frequency grid for later analysis. The optical cavity was included in the simulations using the radiation-reaction potential [22, 23], implemented in a publicly available branch of GPAW [24].

For the computation of HCs, including projections on the molecule, we used the method of Refs. 1, 25, which is implemented in the rhodent package [26]. Details are found in the references. In short, we post process the saved Fourier transform the the KS density matrices to calculate the response to a Gaussian pulse

$$\mathcal{E}_z(t) = \mathcal{E}_0 \cos(\omega_0 t) \exp(-(t-t_0)^2/\tau_0^2) \tag{S1}$$

of frequency ω_0, strength $\mathcal{E}_0 = 51\,\mathrm{\mu V\,Å^{-1}}$, peak time $t_0 = 10$ fs, and duration $\tau_0 = 2.1$ fs (corresponding to a FWHM in frequency space of 0.7 eV). Because the number of electrons injected to the molecule does not reach a steady state, we present values that are averages in the time window between 25 and 30 fs in the simulation (see Fig. S3).

We computed the total density of states as

$$\sum_k \delta(\varepsilon - \varepsilon_k) \tag{S2}$$

and the PDOS for the molecule as

$$\sum_k \delta(\varepsilon - \varepsilon_k) \int_{\mathrm{mol}} \left|\phi_k^{(0)}(\boldsymbol{r})\right|^2 \mathrm{d}\boldsymbol{r}, \tag{S3}$$

where ε_k and $\phi_k^{(0)}(\boldsymbol{r})$ are the KS eigenvalues and wave functions, and the integral goes over the Voronoi region of the molecule (that is each point in space which is closer

to the molecule than any other atom). For visualization, the δ-functions in energy were replaced by a Gaussian $(2\pi\sigma^2)^{-1/2}\exp(-\varepsilon^2/2\sigma^2)$ with width $\sigma = 0.07\,\mathrm{eV}$.

[1] J. Fojt, T. P. Rossi, M. Kuisma, and P. Erhart, Hot-Carrier Transfer across a Nanoparticle–Molecule Junction: The Importance of Orbital Hybridization and Level Alignment, Nano Lett. **22**, 8786 (2022).

[2] G. Kresse and J. Hafner, Ab initio molecular dynamics for liquid metals, Phys. Rev. B **47**, 558 (1993).

[3] G. Kresse and J. Furthmüller, Efficient iterative schemes for ab initio total-energy calculations using a plane-wave basis set, Phys. Rev. B **54**, 11169 (1996).

[4] G. Kresse and J. Furthmüller, Efficiency of ab-initio total energy calculations for metals and semiconductors using a plane-wave basis set, Nato. Sc. S. Ss. Iii. C. S. **6**, 15 (1996).

[5] P. E. Blöchl, Projector augmented-wave method, Phys. Rev. B **50**, 17953 (1994).

[6] G. Kresse and D. Joubert, From ultrasoft pseudopotentials to the projector augmented-wave method, Phys. Rev. B **59**, 1758 (1999).

[7] M. Dion, H. Rydberg, E. Schröder, D. C. Langreth, and B. I. Lundqvist, Van der Waals Density Functional for General Geometries, Phys. Rev. Lett. **92**, 246401 (2004).

[8] K. Berland and P. Hyldgaard, Exchange functional that tests the robustness of the plasmon description of the van der Waals density functional, Phys. Rev. B **89**, 035412 (2014).

[9] J. Klimeš, D. R. Bowler, and A. Michaelides, Chemical accuracy for the van der Waals density functional, J. Phys. Condens. Matter **22**, 022201 (2009).

[10] G. Román-Pérez and J. M. Soler, Efficient Implementation of a van der Waals Density Functional: Application to Double-Wall Carbon Nanotubes, Phys. Rev. Lett. **103**, 096102 (2009).

[11] A. H. Larsen, J. J. Mortensen, J. Blomqvist, I. E. Castelli, R. Christensen, M. Dułak, J. Friis, M. N. Groves, B. Hammer, C. Hargus, E. D. Hermes, P. C. Jennings, P. B. Jensen, J. Kermode, J. R. Kitchin, E. L. Kolsbjerg, J. Kubal, K. Kaasbjerg, S. Lysgaard, J. B. Maronsson, T. Maxson, T. Olsen, L. Pastewka, A. Peterson, C. Rostgaard, J. Schiøtz, O. Schütt, M. Strange, K. S. Thygesen, T. Vegge, L. Vilhelmsen, M. Walter, Z. Zeng, and K. W. Jacobsen, The atomic simulation environment—a Python library for working with atoms, J. Phys. Condens. Matter **29**, 273002 (2017).

[12] J. J. Mortensen, L. B. Hansen, and K. W. Jacobsen, Real-space grid implementation of the projector augmented wave method, Phys. Rev. B **71**, 035109 (2005).

[13] J. J. Mortensen, A. H. Larsen, M. Kuisma, A. V. Ivanov, A. Taghizadeh, A. Peterson, A. Haldar, A. O. Dohn, C. Schäfer, E. Ö. Jónsson, E. D. Hermes, F. A. Nilsson, G. Kastlunger, G. Levi, H. Jónsson, H. Häkkinen, J. Fojt, J. Kangsabanik, J. Sødequist, J. Lehtomäki, J. Heske, J. Enkovaara, K. T. Winther, M. Dulak, M. M. Melander, M. Ovesen, M. Louhivuori, M. Walter, M. Gjerding, O. Lopez-Acevedo, P. Erhart, R. Warmbier, R. Würdemann, S. Kaappa, S. Latini, T. M. Boland, T. Bligaard, T. Skovhus, T. Susi, T. Maxson, T. Rossi, X. Chen, Y. L. A. Schmerwitz, J. Schiøtz, T. Olsen, K. W. Jacobsen, and K. S. Thygesen, GPAW: An open Python package for electronic structure calculations, J. Chem. Phys. **160**, 092503 (2024).

[14] A. H. Larsen, M. Vanin, J. J. Mortensen, K. S. Thygesen, and K. W. Jacobsen, Localized atomic basis set in the projector augmented wave method, Phys. Rev. B **80**, 195112 (2009).

[15] M. Kuisma, A. Sakko, T. P. Rossi, A. H. Larsen, J. Enkovaara, L. Lehtovaara, and T. T. Rantala, Localized surface plasmon resonance in silver nanoparticles: Atomistic first-principles time-dependent density-functional theory calculations, Phys. Rev. B **91**, 115431 (2015).

[16] O. Gritsenko, R. van Leeuwen, E. van Lenthe, and E. J. Baerends, Self-consistent approximation to the Kohn-Sham exchange potential, Phys. Rev. A **51**, 1944 (1995).

[17] M. Kuisma, J. Ojanen, J. Enkovaara, and T. T. Rantala, Kohn-Sham potential with discontinuity for band gap materials, Phys. Rev. B **82**, 115106 (2010).

[18] S. Lehtola, C. Steigemann, M. J. T. Oliveira, and M. A. L. Marques, Recent developments in libxc — A comprehensive library of functionals for density functional theory, SoftwareX **7**, 1 (2018).

[19] A. Castro, A. Rubio, and M. J. Stott, Solution of Poisson's equation for finite systems using plane-wave methods, Can. J. Phys. **81**, 1151 (2003).

[20] P. Pulay, Convergence acceleration of iterative sequences. the case of scf iteration, Chem. Phys. Lett. **73**, 393 (1980).

[21] K. Yabana and G. F. Bertsch, Time-dependent local-density approximation in real time, Phys. Rev. B **54**, 4484 (1996).

[22] C. Schäfer and G. Johansson, Shortcut to self-consistent light-matter interaction and realistic spectra from first principles, Phys. Rev. Lett. **128**, 156402 (2022).

[23] C. Schäfer, Polaritonic chemistry from first principles via embedding radiation reaction, The Journal of Physical Chemistry Letters **13**, 6905 (2022), pMID: 35866694, https://doi.org/10.1021/acs.jpclett.2c01169.

[24] Public GPAW fork `https://gitlab.com/christian.schaefer.physics/gpaw/-/tree/qed/`. Please note that the implementation is experimental and the API is subject to change.

[25] T. P. Rossi, P. Erhart, and M. Kuisma, Hot-Carrier Generation in Plasmonic Nanoparticles: The Importance of Atomic Structure, Acs Nano **14**, 9963 (2020).

[26] J. Fojt, T. Rossi, and P. Erhart, rhodent – Analyzing hot-carrier distributions from TD-DFT simulations (2024), accessed: 2024-09-07.